American Mineralogist, Volume 88, pages 556–566, 2003

Topology of the pyroxenes as a function of temperature, pressure, and composition as determined from the procrystal electron density

ROBERT T. DOWNS*

Department of Geosciences, University of Arizona, Tucson, Arizona 85721-0077, U.S.A.

ABSTRACT

The distribution of bonds associated with the M2 sites in various well-ordered pyroxene minerals is determined using a topological analysis of electron density in the manner proposed by Bader (1998). Each M2 atom is bonded to 2 O1 and to 2 O2 atoms, and to zero, one, two, or four bridging O3 atoms. Each of the symmetries displayed by pyroxenes have their own bonding systematics, and each pyroxene-to-pyroxene phase transition involves a change in bonding to M2. As a function of temperature or pressure, the bonding changes appear as a well-defined sequence of steps that can be related to the degree of distortion from the ideal closest packing of anions. It is proposed that the condition at which an individual phase transition occurs is related to M2-Si repulsion through a shared edge. The bonding analysis should provide a qualitative means to interpret the behavior of all pyroxene structures over *T*, *P*, and *x*, and may guide the interpretation of the changes in properties observed by techniques other than X-ray diffraction, such as Raman spectroscopy.

INTRODUCTION

The first pyroxene structure to be determined was *C*2/*c* diopside, $CaMgSi_2O_6$, which was followed two years later with the determination of the structure of *Pbca* hypersthene, $MgSiO_3$ (Warren and Bragg 1928; Warren and Modell 1930). These classic studies established that parallel chains of edge-sharing $M1O_6$ octahedral groups and corner-sharing SiO_4 tetrahedral groups are the common skeletal components of all pyroxenes structures. Two decades later, Ito (1950) predicted the existence of a $P2_1/c$ structure and suggested that *Pbca* orthopyroxene was a "space group twin" of this structure. Ten years later, Morimoto et al. (1960) reported the crystal structures of clinoenstatite and pigeonite in $P2_1/c$ symmetry. About the same time, Smith (1959) determined the structure of a *Pbcn* protopyroxene. Thompson (1970) derived a number of ideal pyroxenes based upon anion closest-packing considerations and, among other things, determined that the ideal form of the *Pbcn* structure exhibits $P2_1cn$ symmetry. Recently, Yang et al. (1999) observed a new pyroxene structure with $P2_1cn$ symmetry when pressure was applied to the *Pbcn* protopyroxene $Mg_{1.54}Li_{0.23}Sc_{0.23}Si_2O_6$.

Along with these original studies, the structures of a large number of pyroxenes have been determined, and transformations involving symmetry changes have been documented as a function of temperature, pressure, and composition. For instance, kanoite ($MnMgSi_2O_6$) transforms from $P2_1/c$ to *C*2/*c* with increasing temperature, (Arlt and Armbruster 1997), spodumene ($LiAlSi_2O_6$) transforms from *C*2/*c* to $P2_1/c$ with increasing pressure (Arlt and Angel 2000), and the symmetry of $(Ca,Mg)MgSi_2O_6$ was observed to change from *C*2/*c* to $P2_1/c$ along the diopside-enstatite join with increasing Mg content (Tribaudino 2000). For a more general discussion and summary of the structure types and crystal chemistry of the pyroxenes, the reader is referred to Bragg et al. (1965), Papike et al. (1973), Cameron and Papike (1981), Deer et al. (1997), as well as Yang and Prewitt (2000).

As reviewed by Pannhorst (1981), the gross topological features of pyroxenes can be described by the stacking sequences of the octahedral and tetrahedral layers. The variety of sequences can be summarized by observing the "skew", "tilt", or direction of stagger of the octahedral layers (Cameron and Papike 1981). This is illustrated in Figure 1 for the four main symmetries adopted by the pyroxenes. The octahedra labeled with "+" are oriented in a direction common to each other, while the octahedra labeled with "–" are oriented in the opposite direction from those labeled with "+". Only transformations involving symmetry changes between *C*2/*c* and $P2_1/c$ and between *Pbcn* and $P2_1cn$ have been observed that do not change these stacking sequences. The mechanism for stacking changes is not completely understood, but it clearly requires extensive changes in the M1-O and M2-O bonded interactions (Coe and Kirby 1975; Yamanaka et al. 1985; Kanzaki 1991).

In some cases, single crystals are shattered by the transformations that involve a change in the stacking sequence. For example, a single crystal of orthoferrosilite turned to powder when it transformed at high pressure to *C*2/*c* clinoferrosilite (Hugh-Jones et al. 1996). However, in other cases the crystals remain intact. For example, a single crystal of orthoferrosilite remained intact when it transformed to clinoferrosilite with increasing temperature (Sueno et al. 1984), and a single crystal of enstatite was preserved through ortho-clino-proto transformations when heated and quenched (Smyth 1974a). After go-

* E-mail: downs@geo.arizona.edu

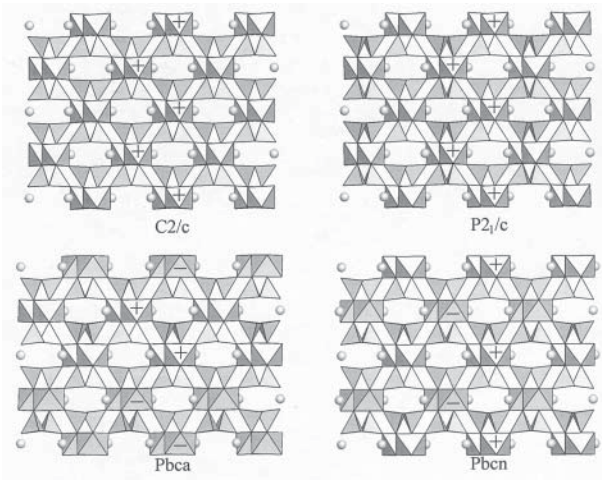

FIGURE 1. The stacking sequences of octahedral and tetrahedral layers for the four main symmetries adopted by pyroxenes. The variety of stacking sequences can be summarized by observing the "skew", "tilt" or direction of stagger of the octahedral layers (Cameron and Papike 1981). The octahedra labeled "+" are oriented in a common direction, while the octahedra labeled "–" are oriented in the opposite direction.

ing through the transformations the crystals are usually twinned and/or display stacking faults. These sorts of observations prompted Ito to remark, "untwinned clinoenstatite can only be obtained by direct crystallization from melt, but not through solid-solid phase transitions…" (Ohashi 1984).

Sueno et al. (1984) recognized the importance of bonding to the M2 atom. In their study of the high-temperature transition of *Pbca* orthoferrosilite to *C2/c* clino-ferrosilite, they say, "It is probable that the thermal behavior of the M2 atom, especially in bonding with the O3 atoms, is most important for the pyroxene transition. The switching of the O3 atoms may bring about a spatial imbalance in the distribution of bonds around the M2 atom in the orthopyroxene structure and this imbalance may become one of the motive forces for the ortho-clino transition." Further on they also say, "In the analysis of the mechanism of the pyroxene transition, the study of the bonding distribution around the M2 site, including the electrical charge and the interatomic angles, may be important in addition to the details of the bond lengths of the M2 polyhedron." However, at the time of the Sueno et al. (1984) study there was no unambiguous way to determine bonding topologies around the M2 atoms, and little has been done to determine the bond distributions.

DETERMINATION OF BOND DISTRIBUTIONS

Recently, Bader (1990) and his colleagues proposed a strategy for analyzing the topology of molecules and crystals in terms of the distribution of critical points in the electron density. These are points at which the gradient of the electron density is zero. These points include (1) maxima, which are located at the positions of the atoms, (2) minima, and (3) saddle points. In particular, Bader (1998) points out that a pair of atoms is bonded if and only if there exists a bond path and a saddle point in the electron density between that pair of atoms. A bond path is a line, not necessarily straight, with the property that the electron density at each point along its length is a local maximum in the perpendicular plane. The saddle point, referred to as a bond critical point (bcp), is the point of local minimum along the bond path. Two different electron density contour maps around the Na atom in jadeite are presented in Figure 2. The two maps can be compared to illustrate the topological features used to determine whether a pair of atoms is bonded or not. The determination of the location of bcp's in a crystal provides coordination numbers for the various atoms in the structure, as well as a topological classification. Associated with each bcp is (1) the value of the electron density at that point, ρ, related to the bond strength (Gibbs et al. 2001) and (2) the value of the Laplacian ($-\nabla^2\rho$), related to the bond character (Bader 1990).

In general, determination of the electron density of a crystal can be a labor-intensive experiment, as exemplified by Kuntzinger et al. (1999) for spodumene, or a time-consuming calculation (Coppens 1997). However, in a study of more than 300 cation-O atom bonds in minerals, Downs et al. (2002) recently showed that every bcp found from experiment or first-principles quantum calculations was also found in the procrystal electron density. The procrystal representation of the electron density distribution of a crystal is constructed by superimposing spherically averaged electron density distributions of static, ground state neutral atoms at the positions that they occupy in the crystal. The calculations are simple and fast: on a 300 MHz PC it takes less than 1 minute to determine the locations and properties of the bcp's around the M2 site in a pyroxene structure. The procrystal calculations not only reproduce the locations of the bcp's, but they also provide a meaningful measure of other bcp properties, especially the magnitude of the electron density and its first and second derivatives, that vary systematically with those obtained in first-principles calculations. In particular, Downs et al. (2002) computed the bonding topologies of the *C2/c* and *P*2$_1$*/c* pyroxenes ferrosilite ($FeSiO_3$) and kanoite ($MnMgSi_2O_6$) with both the procrystal and first-principles models and obtained identical results. They concluded that the procrystal model is an especially useful tool for the accurate determination of bonding topologies. Brown (2002) has presented an argument that explains the success of the procrystal model in determining the bonding topology of a crystal.

In this paper, the procrystal electron density is used to determine the bonding around the *M2* atoms in a variety of pyroxene structures; these are listed in Table 1. A pair of atoms is considered bonded if an associated bond critical point in the procrystal electron density is found between the pair. Only structures without mixed occupancies can be examined in a meaningful way with the procrystal model, so the analysis is only performed on ordered pyroxenes with end-member compositions. The various bonding topologies are classified and systematics of transformations between pyroxenes are discussed. In a mathematical sense, the description of the "topology" of a three dimensional network means the description of the distribution of nodes and lines that connect the nodes. In this paper, the description of the topology of the pyroxenes means a description of the position of the atoms (nodes) and the bonds (lines) that join them together.

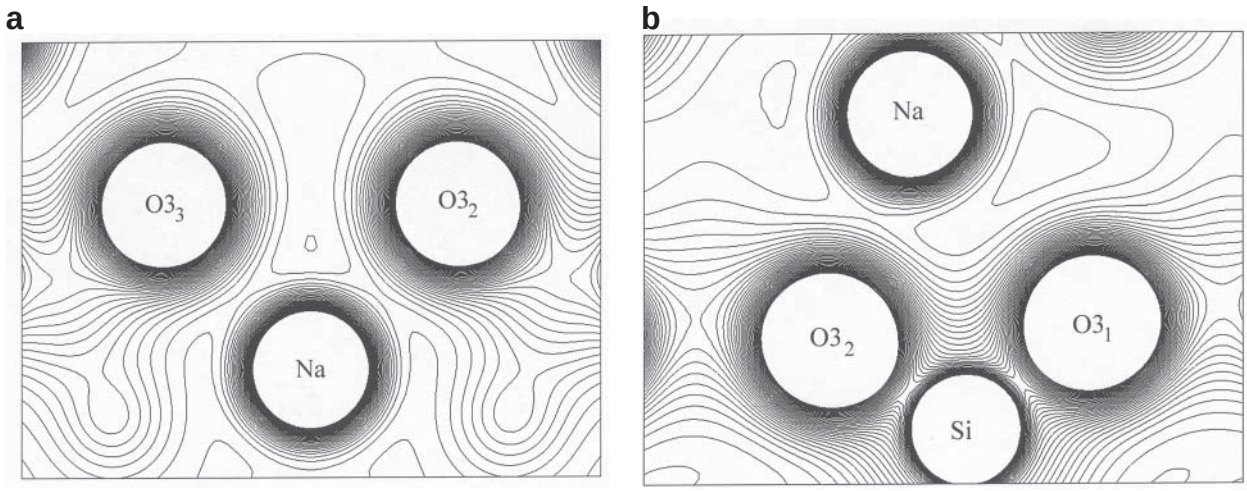

FIGURE 2. A plane of procrystal electron density for jadeite, $NaAlSi_2O_6$, computed from the structural data of Clark et al. (1969). Contour lines are displayed from 0 £ r £ 0.2 e/Å^3 at 0.005 intervals. This figure illustrates the distribution of the electron density between sodium and the bonded and non-bonded bridging O atoms. If a saddle point exists in the electron density between the Na and O atoms, then the atoms are bonded. (**a**) In the plane that includes Na and its two bonded bridging atoms, $O3_2$ and $O3_3$. The figure is 6.28 Å ¥ 4.71 Å in dimension. (**b**) In the plane that includes Na, non-bonded $O3_1$, and bonded $O3_2$. This figure is 6.00 Å ¥ 4.50 Å in dimension.

TOPOLOGIES OF THE PYROXENES

Parallel chains of edge-sharing $M1O_6$ groups and corner-sharing SiO_4 groups are the common skeletal components of all pyroxenes structures. One of the major differences between pyroxene structures is the bond distribution involving the M2 atom. It is always bonded to four O atoms (2 ¥ O1 + 2 ¥ O2) that are also bonded to M1. However, the M2 atom can have up to four more bonds with neighboring bridging O3 atoms. The existence and distribution of these bonds is a function of temperature, pressure, and chemistry, and correlates, to some extent, with the space group symmetry of a particular structure.

For the purposes of this study it is convenient to determine a standard orientation for the pyroxene structure. I define this orientation using the *C2/c* pyroxene structure as shown in Figure 3. The key to this orientation is the relationship between the positions of the M2 atoms and the chains of neighboring M1 octahedra. Standardizing this orientation ensures a common orientation of the octahedral chains such that the bonds between M2 and the O1 and O2 atoms of the octahedral chain are both geometrically and topologically identical from structure to structure. There are four bridging O3 atoms that neighbor the M2 atom, to which they can bond. I label these $O3_1$ through $O3_4$ and they are distributed as shown in Figure 3. If a *C2/c* structure is examined in this orientation, then the same M2-O3 topologies exist, whether the structure is viewed down **a*** or –**a***. This orientation is the same as that adopted by Sueno et al. (1976).

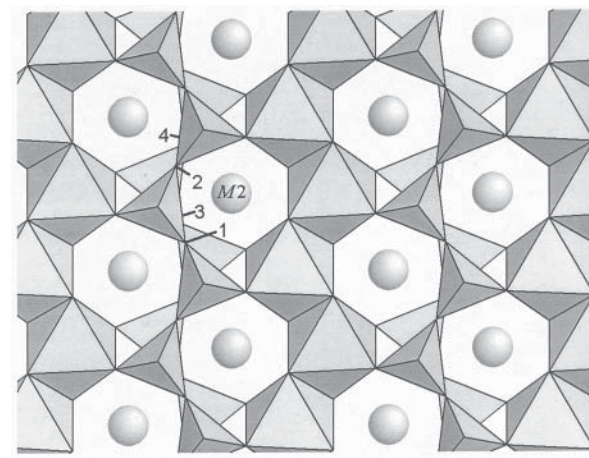

FIGURE 3. The pyroxene skeleton, with edge-sharing chains of $M1O_6$ octahedra parallel to corner-sharing chains of tetrahedra. The M2 site is displayed as a sphere. The orientation of the figure is chosen such that the octahedral chains are oriented as shown, with an "arrowhead" made of two faces pointing at 2 o'clock from the labeled M2 site. Subscripts of the four bridging O3 atoms are indicated on the image, with $O3_1$ and $O3_2$ above $O3_3$ and $O3_4$. This image was taken from *C2/c* jadeite, looking down **a***, with the **c**-axis vertical, 20 Å in width.

Topology of *C2/c* pyroxenes

I begin with *C2/c* pyroxene because this topology provides a standard model for the discussion of the topologies of pyroxenes of other symmetries. Considering the number of symmetry elements per volume, the *C2/c* structure displays the highest symmetry observed for pyroxenes. Furthermore, in the *C2/c* structures, the M2 atom occurs on a twofold rotation axis, its highest symmetry position among the pyroxene structures. This position constrains its coordination numbers to four, six, or eight. In other pyroxenes the M2 atom may occupy a general position, which places no constraints on its coordination number.

There are four unique topologies displayed by the *C2/c* pyroxenes, one in which the M2 atom is four-coordinated, two in

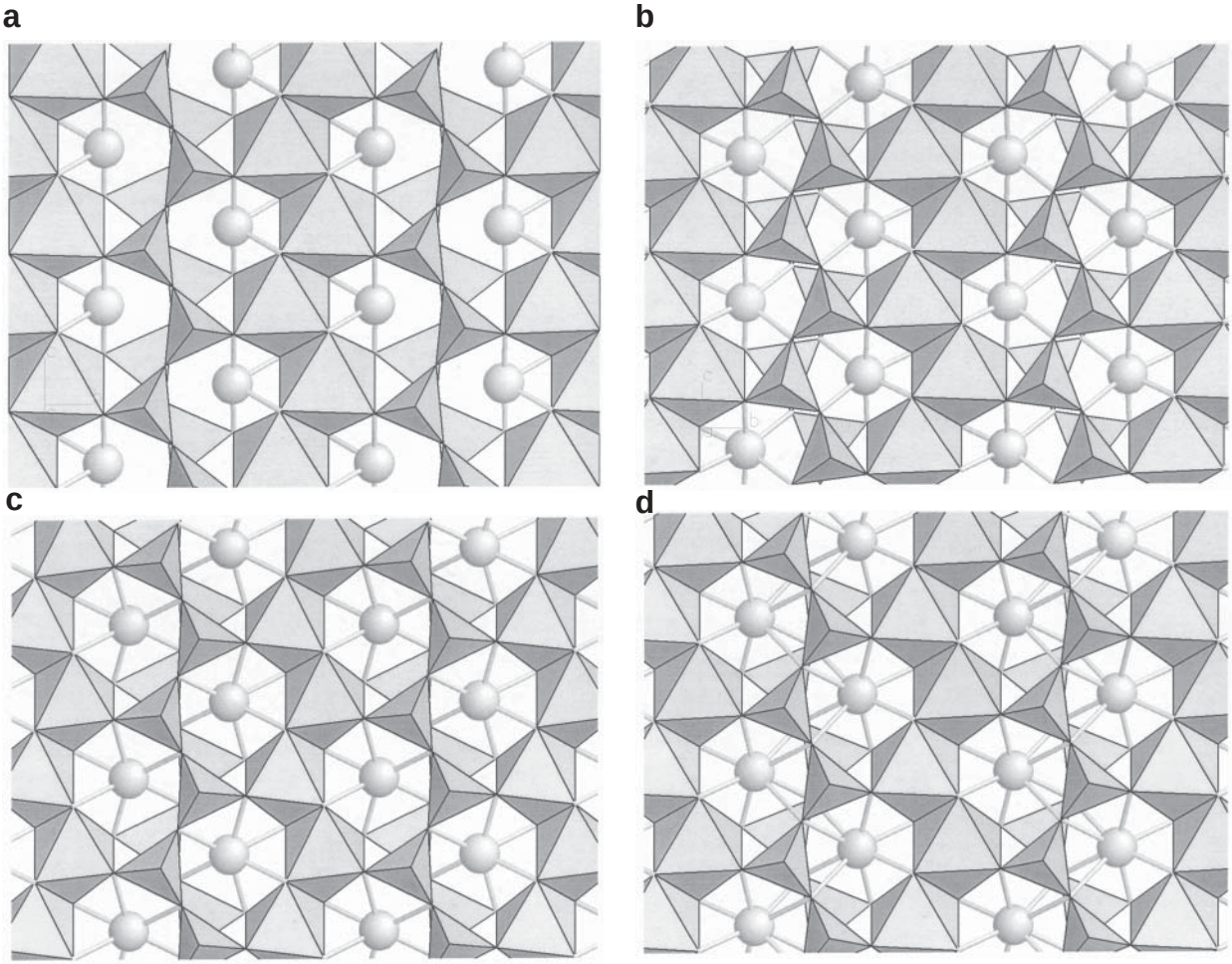

FIGURE 4. Topology of *C*2/*c* pyroxenes. (**a**) Ferrosilite, $FeSiO_3$, at high temperature. The Fe2 atom is not bonded to any bridging O3 atoms. (**b**) Ferrosilite at high pressure. The Fe2 atom is bonded to two bridging O3 atoms, $O3_1$ and $O3_4$. This topology has only been observed for pyroxenes at high-pressure. (**c**) Jadeite, $NaAlSi_2O_6$, at room conditions. The Na2 atom is bonded to two bridging O3 atoms, $O3_2$ and $O3_3$. This represents the most common topology for *C*2/*c* pyroxenes. (**d**) Diopside, $CaMgSi_2O_6$, at room conditions. The Ca2 atom is bonded to all four bridging O3 atoms.

which it is six-coordinated, and one that is eight-coordinated, as exemplified by the following structures. In clino-ferrosilite (Sueno et al. 1984) at 1050 °C, the procrystal electron density indicates that the Fe2 atom is bonded only to O1 and O2 atoms, and not to any of the bridging O3 atoms (Fig. 4a). In clino-ferrosilite (Hugh-Jones et al. 1994), at $P > 1.87$ GPa, the Fe2 atom is bonded to two O3 atoms, $O3_1$ and $O3_4$ (Fig. 4b). At present, this particular bonding topology has only been observed in pyroxenes at high pressures. In jadeite (Cameron et al. 1973), Na2 is bonded to the other two O3 atoms, $O3_2$ and $O3_3$ (Fig. 4c). In diopside, (Clark et al. 1969) Ca2 is bonded to all four O3 atoms (Fig. 4d). The bonding topologies of jadeite and diopside are typical of room-condition *C*2/*c* pyroxenes. The bonding patterns of other pyroxenes with *C*2/*c* symmetry are given in Table 1.

One would think that these coordination numbers should systematically follow radii (Arlt et al. 1998), with the coordination number increasing with the radius of the M2 cation, but they do not. For instance, at ambient conditions all Ca is eight-coordinated, while all Na is six coordinated, but their radii are similar. Li is four-coordinated in some *C*2/*c* structures, such as $LiScSi_2O_6$, but six-coordinated in others, such as spodumene ($LiAlSi_2O_6$). Furthermore, there is no correlation between the length of *c* and the coordination number of M2, indicating that there is no correlation with the size of M1. However, a strong correlation exists between the coordination number of M2 and the β cell angle, with larger β angles associated with small coordination number, and smaller β angles associated with larger coordination numbers, as shown in Figure 5. This plot indicates that structures with β angles larger than ~110° have M2 atoms that are not bonded to O3 atoms, and structures with 106° < β < ~110° have M2 atoms bonded to $O3_2$ and $O3_3$. If ~104° < β < 106°, then M2 is bonded to all four O3 atoms, and if β < 104° then M2 is bonded to $O3_1$ and $O3_4$.

Topology of the $P2_1/c$ pyroxenes

The $P2_1/c$ pyroxenes are observed to display two different bonding topologies. The M2 atom is either fivefold coordinated with a bond to $O3_2$, or sixfold coordinated with bonds to $O3_2$

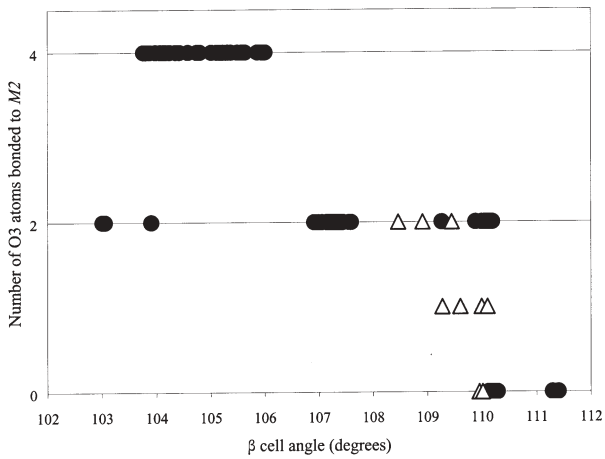

FIGURE 5. A plot showing the β cell angle vs. number of O3 atoms bonded to M2 for the clinopyroxenes listed in Table 1. *C2/c* pyroxenes are indicated by a solid circle, and $P2_1/c$ pyroxenes are indicated by an open triangle. This figure illustrates the strong correlation between the topology of clinopyroxenes and the β cell angle, which is interpreted as indicating a relationship between the distortion in packing of the anions and the coordination of the M2 site in pyroxenes.

and $O3_4$. The coordination number follows the same systematic with the β cell angle as is shown in Figure 5 for the *C2/c* polymorphs.

Of the structures examined, only those with Li at the M2 site display fivefold coordination. This topology (Fig. 6a) is exhibited by $LiAlSi_2O_6$ spodumene at 3.34 GPa (Arlt and Angel. 2000), $LiScSi_2O_6$ at P = 2.11 and 4.80 GPa (Arlt and Angel, 2000), and $LiGaSi_2O_6$ (Sato et al. 1995) and $LiFeSi_2O_6$ (Redhammer et al. 2001) at low T.

Ferrosilite synthesized at 8 GPa and 1200 °C, for example, displays $P2_1/c$ symmetry at room conditions (Hugh-Jones et al. 1994). The Fe2 atom is bonded to 2 bridging O atoms, $O3_2$ and $O3_4$, as shown in Figure 6b.

Unlike the *C2/c* pyroxenes, defining the bonding topology in $P2_1/c$ pyroxenes can be ambiguous. For instance, instead of defining bonds from M2 to $O3_2$ and $O3_4$, if the $P2_1/c$ structure is viewed from –**a*** rather than the +**a*** direction, then the bonds would be defined from M2 to $O3_1$ and $O3_3$. This ambiguity can be resolved by following the bonding changes that occur in pyroxenes such as ferrosilite that transform between *C2/c* and $P2_1/c$ with temperature or pressure, as will be discussed. The bonding patterns of other pyroxenes with $P2_1/c$ symmetry are included in Table 1.

Bragg et al. (1965) stated that the M2 site in $P2_1/c$ pigeonites is seven-coordinated. I am unable to determine the bonding topology around the M2 site in pigeonite with the procrystal model because of compositional variation. However, it is likely that when Mg or Fe occupies the M2 site then it is six-coordinated, and when Ca occupies the site, then it is eight-coordinated. The seven-coordinated M2 site is thus, at best, an average value, not displayed by any individual atom.

Topology of the *Pbca* pyroxenes

In this study I examined $MgSiO_3$, $FeSiO_3$, $CoSiO_3$, and $ZnSiO_3$ orthopyroxenes with *Pbca* symmetry. In the first three

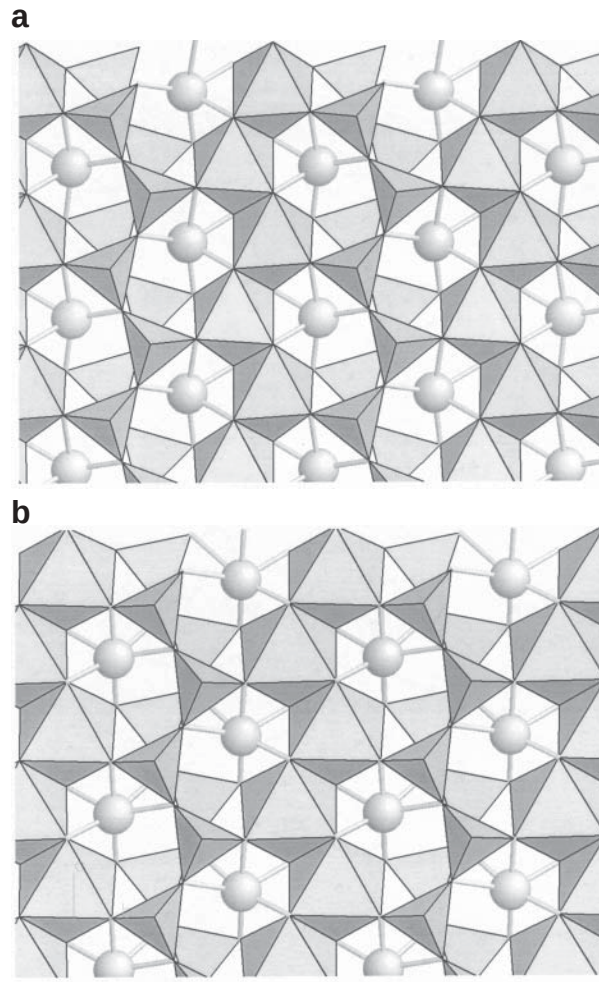

FIGURE 6. Topology of $P2_1/c$ pyroxenes. (**a**) Spodumene, $LiAlSi_2O_6$, at 3.342 GPa. The Li2 atom is bonded only to one bridging O3 atom. (**b**) Ferrosilite, $FeSiO_3$, at room conditions. The Fe2 atom is bonded to two bridging O3 atoms.

cases the M2 atom is bonded to two bridging atoms, $O3_2$ and $O3_4$, while Zn2 is bonded only to $O3_2$. Bonding details are found in Table 1 and illustrations are in Figure 7. Labeling the bonding topology of the *Pbca* pyroxenes is similar in ambiguity to the case of the $P2_1/c$ pyroxenes. By changing the direction of view, say along –**a*** instead of along +**a***, then the M2 bonds could be defined as to $O3_1$ and $O3_3$ instead of $O3_2$ and $O3_4$. But unlike for the $P2_1/c$ pyroxenes, this ambiguity does not appear to be resolved by following the transformation to *C2/c* because of stacking sequence changes. At high pressures the symmetry of both $MgSiO_3$ and $FeSiO_3$ changes from *Pbca* to *C2/c* (Angel et al. 1992; Hugh-Jones et al. 1996). The structure has not yet been determined for the *C2/c* phases, so the bonding sequences can only be extrapolated from observing trends in the changes of packing of the anions observed at T or P. These trends are discussed below in greater detail.

In their study of the high-temperature behavior of orthoferrosilite, Sueno et al. (1976) stated that the coordination number of Fe2 increases from six at 24 °C to seven between 600 °C and 800 °C and then back to six again at higher

TABLE 1. Identification of *M*2 – O3 bonds and associated critical point properties of the procrystal electron density

Phase	M2	O3 bonds	*R* (M2O) Å	ρ (M2) Å	ρ (O) Å	ρ e/Å^3	$\Delta^2\rho$ e/Å^5	Reference
spodumene, *C*2/*c*	Li	2,3	2.251	0.847	1.412	.08821	1.8503	a
spodumene, *T* = 24 °C, *C*2/*c*	Li	2,3	2.253	0.847	1.413	.08790	1.8407	b
spodumene, *T* = 300 °C, *C*2/*c*	Li	2,3	2.268	0.852	1.425	.08572	1.7604	b
spodumene, *T* = 460 °C, *C*2/*c*	Li	2,3	2.286	0.858	1.440	.08307	1.6619	b
spodumene, *T* = 760 °C, *C*2/*c*	Li	2,3	2.296	0.861	1.447	.08160	1.6119	b
spodumene, *P* = 0 GPa, *C*2/*c*	Li	2,3	2.249	0.846	1.410	.08843	1.8616	c
spodumene, *P* = 3.164 GPa, *C*2/*c*	Li	2,3	2.216	0.835	1.386	.09466	2.0674	c
spodumene, *P* = 3.342 GPa, *P*2$_1$/*c*	Li	2	2.150	0.816	1.341	.10733	2.5016	c
spodumene, *P* = 8.835 GPa, *P*2$_1$/*c*	Li	2	2.085	0.795	1.295	.12429	3.0626	c
	Li	4	2.316	0.874	1.445	.07964	1.4912	c
$LiScSi_2O_6$, *C*2/*c*	Li	none	-	-	-	-	-	d
$LiScSi_2O_6$, *P* = 2.113 GPa, *P*2$_1$/*c*	Li	2	2.418	0.9202	1.513	.05248	0.9319	c
$LiScSi_2O_6$, *P* = 4.804 GPa, *P*2$_1$/*c*	Li	2	2.341	0.8897	1.454	.05947	1.2269	c
$LiFeSi_2O_6$, *C*2/*c*	Li	none	-	-	-	-	-	a
$LiFeSi_2O_6$, *T* = 100 K, *P*2$_1$/*c*	Li	2	2.355	0.8925	1.462	.05510	1.1376	x
$LiFeSi_2O_6$, *T* = 200 K, *P*2$_1$/*c*	Li	2	2.381	0.9012	1.479	.05262	1.0399	x
$LiFeSi_2O_6$, *T* = 298 K, *C*2/*c*	Li	none	-	-	-	-	-	x
$LiFeSi_2O_6$, *T* = 1023 K, *C*2/*c*	Li	none	-	-	-	-	-	x
$LiGaSi_2O_6$, *C*2/*c*	Li	none	-	-	-	-	-	e
$LiGaSi_2O_6$, low *T*, *P*2$_1$/*c*	Li	2	2.341	0.890	1.452	.06197	1.2333	f
jadeite, *C*2/*c*	Na	2,3	2.363	1.077	1.287	.13074	2.6962	a
jadeite, *T* = 24 °C, *C*2/*c*	Na	2,3	2.366	1.079	1.289	.12976	2.6718	b
jadeite, *T* = 400 °C, *C*2/*c*	Na	2,3	2.374	1.082	1.294	.12726	2.6091	b
jadeite, *T* = 600 °C, *C*2/*c*	Na	2,3	2.377	1.083	1.295	.12617	2.5843	b
jadeite, *T* = 800 °C, *C*2/*c*	Na	2,3	2.383	1.085	1.299	.12447	2.5407	b
$NaScSi_2O_6$, *C*2/*c*	Na	2,3	2.460	1.115	1.349	.10638	2.0189	g
$NaScSi_2O_6$, *C*2/*c*	Na	2,3	2.460	1.115	1.349	.10653	2.0215	h
acmite, *C*2/*c*	Na	2,3	2.430	1.103	1.329	.11254	2.2127	a
acmite, *T* = 400 °C, *C*2/*c*	Na	2,3	2.438	1.106	1.334	.11039	2.1597	b
acmite, *T* = 600 °C, *C*2/*c*	Na	2,3	2.446	1.109	1.339	.10836	2.1075	b
acmite, *T* = 800 °C, *C*2/*c*	Na	2,3	2.450	1.111	1.342	.10728	2.0819	b
kosmochlor, *C*2/*c*	Na	2,3	2.424	1.100	1.326	.11585	2.2667	a
kosmochlor, *T* = 24 °C, *C*2/*c*	Na	2,3	2.427	1.102	1.328	.11489	2.2412	b
kosmochlor, *T* = 400 °C, *C*2/*c*	Na	2,3	2.440	1.107	1.336	.11170	2.1589	b
kosmochlor, *T* = 600 °C, *C*2/*c*	Na	2,3	2.434	1.104	1.332	.11268	2.1927	b
kosmochlor, *P* = 0 GPa, *C*2/*c*	Na	2,3	2.419	1.099	1.323	.11681	2.2945	cc
kosmochlor, *P* = 5.78 GPa, *C*2/*c*	Na	2,3	2.422	1.098	1.327	.11966	2.3060	cc
kosmochlor, *P* = 9.75 GPa, *C*2/*c*	Na	2,3	2.406	1.092	1.318	.12543	2.4303	cc
		1,4	2.596	1.170	1.445	.08565	1.3697	
$NaInSi_2O_6$, *C*2/*c*	Na	2,3	2.510	1.133	1.384	.09709	1.7583	y
enstatite, *Pbca*	Mg	2	2.288	1.005	1.300	.18110	2.3699	i
		4	2.447	1.078	1.369	.13763	1.2197	
enstatite, *Pbca*	Mg	2	2.289	1.005	1.300	.18114	2.3660	j
		4	2.448	1.079	1.370	.13748	1.2145	
enstatite, *P* = 0 GPa, *Pbca*	Mg	2	2.297	1.009	1.307	.17902	2.2841	k
		4	2.457	1.083	1.374	.13605	1.1723	
enstatite, *P* = 1.04 GPa, *Pbca*	Mg	2	2.280	1.001	1.296	.18415	2.4471	k
		4	2.403	1.057	1.347	.14586	1.4662	
enstatite, *P* = 1.95 GPa, *Pbca*	Mg	2	2.253	0.989	1.274	.19079	2.7284	k
		4	2.381	1.046	1.335	.15037	1.6088	
enstatite, *P* = 3.27 GPa, *Pbca*	Mg	2	2.258	0.991	1.278	.19022	2.6825	k
		4	2.344	1.030	1.314	.15834	1.8649	
enstatite, *P* = 4.09 GPa, *Pbca*	Mg	2	2.256	0.991	1.278	.19106	2.6974	k
		4	2.333	1.025	1.309	.16116	1.9515	
enstatite, *P* = 4.95 GPa, *Pbca*	Mg	2	2.238	0.983	1.263	.19523	2.8910	k
		4	2.311	1.016	1.296	.16616	2.1220	
enstatite, *P* = 5.85 GPa, *Pbca*	Mg	2	2.226	0.978	1.258	.20053	3.0292	k
		4	2.290	1.006	1.284	.17198	2.3134	
enstatite, *P* = 7.00 GPa, *Pbca*	Mg	2	2.226	0.978	1.257	.20085	3.0356	k
		4	2.230	1.010	1.290	.16985	2.2302	
enstatite, *P* = 8.10 GPa, *Pbca*	Mg	2	2.213	0.973	1.249	.20458	3.1864	k
		4	2.560	0.994	1.266	.18027	2.5954	
protoenstatite, *T* = 1080 °C, *Pbcn*	Mg	none	-	-	-	-	-	l
protoenstatite, *T* = 1260 °C, *Pbcn*	Mg	none	-	-	-	-	-	m
protoenstatite, *T* = 1360 °C, *Pbcnp*	Mg	none	-	-	-	-	-	m
protoenstatite, *T* = 1360 K, *Pbcn*	Mg	none	-	-	-	-	-	bb
protoenstatite, *T* = 1400 K, *Pbcn*	Mg	none	-	-	-	-	-	bb
clinoenstatite, *P*2$_1$/*c*	Mg	2 4	2.280 2.412	1.001 1.061	1.294 1.351	.18379 .14400	2.4487 1.4113	n
diopside, *C*2/*c*	Ca	2,3 1,4	2.561 2.717	1.286 1.357	1.278 1.364	.16068 .11813	2.5083 1.5816	a
diopside, *T* = 10 K, *C*2/*c*	Ca	2,3 1,4	2.557 2.706	1.284 1.352	1.276 1.358	.16221 .12035	2.5372 1.6349	z
diopside, *T* = 24 °C, *C*2/*c*	Ca	2,3 1,4	2.561 2.717	1.286 1.357	1.278 1.365	.16062 .11810	2.5062 1.5815	b
diopside, *T* = 400 °C, *C*2/*c*	Ca	2,3 1,4	2.571 2.750	1.290 1.372	1.284 1.384	.15723 .11199	2.4332 1.4410	b
diopside, *T* = 700 °C, *C*2/*c*	Ca	2,3 1,4	2.578 2.773	1.293 1.382	1.288 1.397	.15495 .10812	2.3857 1.3512	b

TABLE 1—*Continued*

Phase	M2	O3 bonds	*R*(M2O) Å	ρ (M2) Å	ρ (O) Å	ρ e/Å^3	Δ^2ρ e/Å^5	Reference
diopside, *T* = 1000 °C, *C*2/*c*	Ca	2,3 1,4	2.587 2.797	1.297 1.393	1.293 1.411	.15191 .10394	2.3244 1.2581	b
diopside, *T* = 700 °C, *C*2/*c*	Ca	2,3 1,4	2.578 2.779	1.293 1.384	1.288 1.401	.15500 .10728	2.3857 1.3281	o
diopside, *P* = 0 GPa, *C*2/*c*	Ca	2,3 1,4	2.561 2.721	1.286 1.359	1.278 1.366	.16081 .11742	2.5091 1.5667	p
diopside, *P* = 2.36 GPa, *C*2/*c*	Ca	2,3 1,4	2.546 2.671	1.279 1.337	1.270 1.337	.16615 .12761	2.6190 1.8039	p
diopside, *P* = 3.52 GPa, *C*2/*c*	Ca	2,3 1,4	2.545 2.640	1.278 1.323	1.269 1.319	.16728 .13453	2.6338 1.9701	p
diopside, *P* = 4.55 GPa, *C*2/*c*	Ca	2,3 1,4	2.538 2.621	1.275 1.315	1.265 1.308	.16956 .13909	2.6831 2.0776	p
diopside, *P* = 5.30 GPa, *C*2/*c*	Ca	2,3 1,4	2.540 2.609	1.276 1.310	1.266 1.301	.16975 .14221	2.6775 2.1494	p
hedenbergite, *T* = 24 °C, *C*2/*c*	Ca	2,3 1,4	2.627 2.719	1.314 1.358	1.318 1.364	.14338 .11597	2.0929 1.5630	b
hedenbergite, *T* = 400 °C, *C*2/*c*	Ca	2,3 1,4	2.629 2.757	1.315 1.375	1.319 1.386	.14235 .10936	2.0787 1.4066	b
hedenbergite, *T* = 600 °C, *C*2/*c*	Ca	2,3 1,4	2.628 2.778	1.315 1.384	1.318 1.398	.14201 .10591	2.0779 1.3236	b
hedenbergite, *T* = 800 °C, *C*2/*c*	Ca	2,3 1,4	2.629 2.794	1.315 1.391	1.319 1.408	.14143 .10345	2.0707 1.2661	b
hedenbergite, *T* = 900 °C, *C*2/*c*	Ca	2,3 1,4	2.636 2.803	1.318 1.395	1.323 1.413	.13980 .10200	2.0310 1.2337	b
hedenbergite, *T* = 1000 °C, *C*2/*c*	Ca	2,3 1,4	2.640 2.811	1.320 1.399	1.325 1.418	.13877 .10060	2.0089 1.2002	b
hedenbergite, *P* = 0 GPa, *C*2/*c*	Ca	2,3 1,4	2.632 2.721	1.316 1.359	1.321 1.365	.14242 .11557	2.0659 1.5550	q
hedenbergite, *P* = 1.19 GPa, *C*2/*c*	Ca	2,3 1,4	2.629 2.690	1.314 1.345	1.320 1.347	.14383 .12179	2.0901 1.6997	q
hedenbergite, *P* = 2.15 GPa, *C*2/*c*	Ca	2,3 1,4	2.620 2.669	1.310 1.336	1.315 1.335	.14627 .12623	2.1429 1.8026	q
hedenbergite, *P* = 2.75 GPa, *C*2/*c*	Ca	2,3 1,4	2.620 2.653	1.310 1.329	1.315 1.326	.14686 .12995	2.1483 1.8890	q
hedenbergite, *P* = 3.65 GPa, *C*2/*c*	Ca	2,3 1,4	2.612 2.630	1.307 1.320	1.310 1.312	.14866 .13487	2.1921 2.0108	q
hedenbergite, *P* = 4.44 GPa, *C*2/*c*	Ca	2,3 1,4	2.609 2.615	1.305 1.313	1.308 1.304	.15002 .13885	2.2157 2.1031	q
hedenbergite, *P* = 4.83 GPa, *C*2/*c*	Ca	2,3 1,4	2.607 2.612	1.304 1.311	1.307 1.302	.15085 .13979	2.2319 2.1216	q
hedenbergite, *P* = 5.30 GPa, *C*2/*c*	Ca	2,3 1,4	2.604 2.593	1.303 1.303	1.305 1.291	.15171 .14429	2.2522 2.2324	q
hedenbergite, *P* = 6.45 GPa, *C*2/*c*	Ca	2,3 1,4	2.600 2.585	1.301 1.300	1.303 1.287	.15307 .14680	2.2759 2.2884	q
hedenbergite, *P* = 7.63 GPa, *C*2/*c*	Ca	2,3 1,4	2.592 2.560	1.297 1.289	1.298 1.273	.15608 .15392	2.3327 2.4517	q
hedenbergite, *P* = 8.75 GPa, *C*2/*c*	Ca	2,3 1,4	2.588 2.544	1.296 1.282	1.296 1.263	.15762 .15884	2.3607 2.5662	q
hedenbergite, *P* = 9.97 GPa, *C*2/*c*	Ca	2,3 1,4	2.577 2.534	1.291 1.277	1.290 1.257	.16098 .16236	2.4369 2.6452	q
kanoite, *P* = 5.2 GPa, *C*2/*c*	Mn	1,4	2.374	1.190	1.184	.23246	3.1306	r
kanoite, *T* = 200 °C, *P*2$_1$/*c*	Mn	2 4	2.412 2.756	1.207 1.392	1.210 1.365	.22676 .12595	2.8475 1.0895	s
kanoite, *T* = 270 °C, *C*2/*c*	Mn	2,3	2.544	1.274	1.284	.18504	1.9510	s
$MnSiO_3$, *P*2$_1$/*c*	Mn	2 4	2.473 2.732	1.239 1.381	1.245 1.352	.20573 .12777	2.3764 1.1413	aa
ferrosilite, *Pbca*	Fe	2 4	2.453 2.589	1.231 1.305	1.236 1.284	.21717 .16162	2.4409 1.6433	j
ferrosilite, *T* = 23 °C, *Pbca*	Fe	2 4	2.459 2.596	1.234 1.309	1.240 1.287	.21541 .15975	2.4028 1.6113	t
ferrosilite, *T* = 400 °C, *Pbca*	Fe	2 4	2.512 2.699	1.270 1.367	1.280 1.333	.19917 .13595	2.0308 1.2413	t
ferrosilite, *T* = 600 °C, *Pbca*	Fe	2 4	2.557 2.770	1.297 1.409	1.261 1.362	.15872 .12233	1.7450 1.0519	t
ferrosilite, *T* = 800 °C, *Pbca*	Fe	2 4	2.581 2.887	1.311 1.478	1.271 1.411	.15207 .10386	1.6350 0.8203	t
ferrosilite, *T* = 900 °C, *Pbca*	Fe	2 4	2.598 2.960	1.321 1.522	1.278 1.441	.14757 .09442	1.5562 0.7132	t
ferrosilite, *T* = 980 °C, *Pbca*	Fe	2 4	2.699 3.015	1.367 1.556	1.333 1.466	.13595 .08849	1.2413 0.6472	t
clinoferrosilite, *T* = 1050 °C, *C*2/*c*	Fe	none	-	-	-	-	-	u
clinoferrosilite, *P*2$_1$/*c*	Fe	2 4	2.297 2.753	1.150 1.402	1.152 1.351	.28818 .12491	3.8838 1.1026	v
clinoferrosilite, *P* = 1.87 GPa, *C*2/*c*	Fe	1,4	2.430	1.220	1.210	.21096	2.5506	v
$Co_2Si_2O_6$, *Pbca*	Co	2 4	2.388 2.516	1.196 1.266	1.200 1.251	.24227 .18242	2.8760 1.9640	j
$ZnSiO_3$, *C*2/*c*	Zn	none	-	-	-	-	-	w
$ZnSiO_3$, *P* = 0.531 GPa, *C*2/*c*	Zn	none	-	-	-	-	-	c
$ZnSiO_3$, *P* = 4.258 GPa, *P*2$_1$/*c*	Zn	2 4	2.443 2.553	1.226 1.286	1.242 1.268	.22106 .16739	2.3229 1.7249	c
$ZnSiO_3$, *P* = 5.304 GPa, *C*2/*c*	Zn	1,4	2.416	1.209	1.207	.21183	2.4527	c
$ZnSiO_3$, *Pbca*	Zn	2	2.957	1.525	1.433	.08910	0.7505	w

Notes: Column labels are defined as: M2: identification of the chemistry of the atom occupying the M2 site. O3 bonds: identification of the particular bonded O3 atom, as defined in Figure 3. *R*(M2O): M2-O bond length. *r*(M2), *r*(O): bonded radii of M2 and O3, equal to the distance from the atomic centers to the location of the bond critical point. r, D^2r: electron density and its Laplacian at the bond critical point. References: (a) Clark et al. (1969); (b) Cameron et al. (1973); (c) Arlt and Angel (2000); (d) Hawthorne and Grundy (1977); (e) Sato et al. (1994); (f) Sato et al. (1995); (g) Hawthorne and Grundy (1973); (h) Ohashi et al. (1994); (i) Ghose et al. (1986); (j) Sasaki et al. (1982); (k) Hugh-Jones and Angel (1994); (l) Murakami et al. (1982); (m) Murakami et al. (1984); (n) Ohashi (1984); (o) Finger and Ohashi (1976); (p) Levien and Prewitt (1981); (q) Zhang et al. (1997); (r) Arlt et al. (1998); (s) Arlt and Armbruster (1997); (t) Sueno et al. (1976); (u) Sueno et al. (1984); (v) Hugh-Jones et al. (1994); (w) Morimoto et al. (1975); (x) Redhammer et al. (2001); (y) Hawthorne and Grundy (1974); (z) Prencipe et al. (2000); (aa) Tokonami et al., (1979); (bb) Yang and Ghose (1995); (cc) Origlieri et al. (2001).

temperatures. This is not confirmed by the topology of the electron density.

Topology of the *Pbcn* pyroxenes

The only crystal structures of well-ordered end-member protopyroxene reported in the literature are from high-temperature studies. Murakami et al. (1982, 1984) reported the structures of *Pbcn* enstatite at 1080, 1260, and 1360 °C, while Yang and Ghose (1995) reported the structure at 1360 and 1400 K. As illustrated in Figure 8, electron density analysis does not show an Mg2-O3 bond. Since a twofold rotation axis passes through the M2 sites in both *C*2/*c* and *Pbcn* pyroxenes, then the bonding constraints for phases with these two symmetries are similar, and, in principle, the M2 atom could be bonded to 0, 2, or four O3 atoms. Likewise, the bonding constraints for *P*2$_1$/*c* and *Pbca* are also similar, with the major differences being the stacking sequence of the octahedral layers (Fig. 1).

CHANGES IN BOND TOPOLOGY WITH TEMPERATURE AND PRESSURE

Several of the pyroxenes listed in Table 1 adopt different symmetries at different temperatures and pressures. For in-

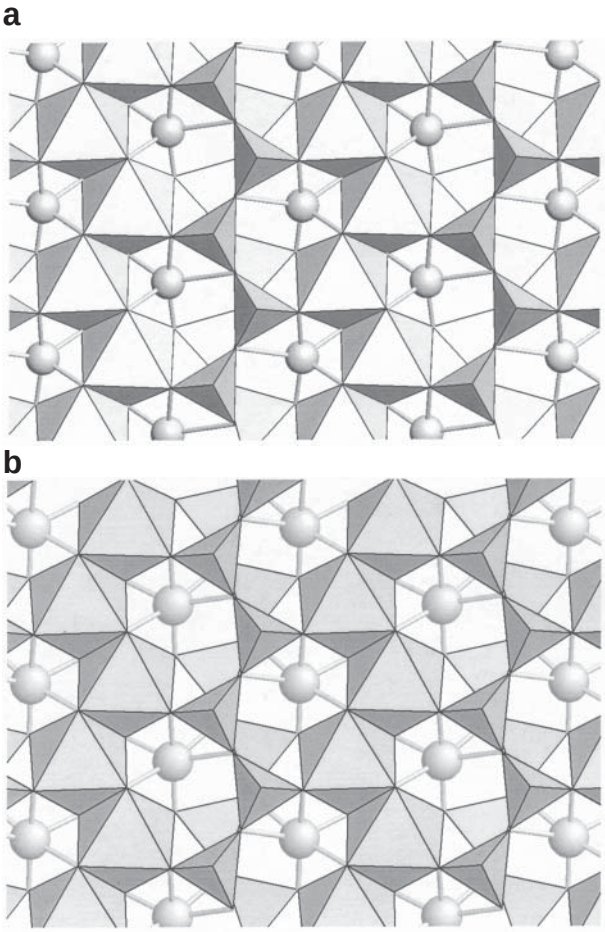

FIGURE 7. Topology of the *Pbca* pyroxenes. (**a**) $ZnSiO_3$ at room conditions. The Zn2 atom is bonded to one bridging O3 atom. The topology around the M2 site is similar to that observed around the five-coordinated M2 site in $P2_1/c$ pyroxenes as illustrated in Figure 6a. (**b**) Orthoferrosilite, $FeSiO_3$, at room conditions. The Fe2 atom is bonded to two bridging O3 atoms, and the topology around the M2 site is similar to that observed around a six-coordinated M2 site in $P2_1/c$ pyroxenes as illustrated in Figure 6b.

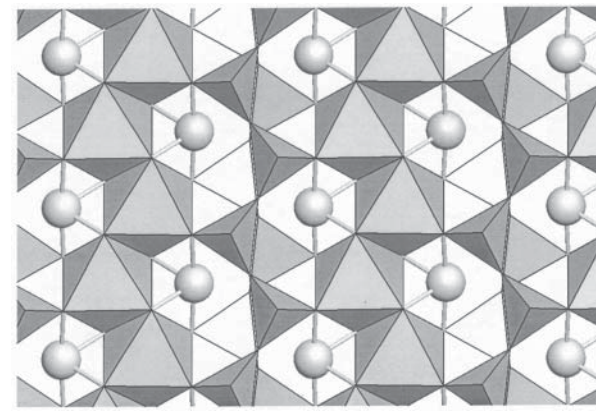

FIGURE 8. Topology of *Pbcn* pyroxene, $MgSiO_3$ protoenstatite, at 1080 °C. The Fe2 atom is not bonded to any bridging O3 atoms. The topology around the M2 site of *Pbcn* pyroxenes is similar to that of the *C2/c* pyroxenes because a twofold rotation axis goes through the M2 site. Thus, even though this lone example of a protopyroxene illustrates a four-coordinated M2 site, the M2 atoms could, in principle, be four, six or eight-coordinated, just like the *C2/c* phases.

stance, $FeSiO_3$ ferrosilite displays *Pbca* symmetry at room conditions (Sueno et al. 1976) (Fig. 7b). If it is heated above ~1000 °C then it adopts *C2/c* symmetry (Sueno et al. 1984) (Fig. 4a). When quenched from *C2/c*, it adopts $P2_1/c$ symmetry (Fig. 6b), which it retains at room conditions (Shimobayashi and Kitamura 1991). Furthermore, if the *Pbca* phase is compressed then it transforms to a twinned *C2/c*, though this particular structure has not yet been determined (Hugh-Jones et al. 1996). If the $P2_1/c$ phase is compressed, then its symmetry changes to *C2/c* (Fig. 4b), but with a "different" structure than the *C2/c* phase found at high *T* (Hugh-Jones et al. 1994).

From the description of the M2-O3 bonding topologies provided above, each change in symmetry is accompanied by a change in the bonding of the M2 atom. In this section of the paper I will outline some of the changes in bond systematics that are related to changes in *T* and *P*. I begin with the *C2/c* – $P2_1/c$ transitions. These are perhaps the simplest to understand because the octahedral stacking sequence is the same in both structures. The transitions of kanoite ($MnMgSi_2O_6$) are especially enlightening. At room conditions Arlt and Armbruster (1997) found that kanoite displayed $P2_1/c$ symmetry (Fig. 6b). From Table 1, Mn2 is bonded to $O3_2$ and $O3_4$ bridging atoms. With an increase in temperature above 240 °C, the symmetry of the structure changes to *C2/c* (Arlt and Armbruster 1997) and Mn2 is bonded to $O3_2$ and $O3_3$ (Fig. 4c). This means that the Mn-$O3_4$ bond broke and the Mn-$O3_3$ bond formed, both on the lower layer in Figure 3, while the Mn-$O3_2$ bond on the upper layer remained intact. Application of pressure to the $P2_1/c$ structure produces a change in symmetry to *C2/c* (Arlt et al. 1998) with Mn2 bonded to $O3_1$ and $O3_4$ (Fig. 4b). This means that the Mn-$O3_4$ bond on the lower layer of Figure 2 remained intact, while on the upper layer the Mn-$O3_2$ bond broke and the Mn-$O3_1$ bond formed. If these three structures are ordered by volume, then we observe a sequence of bonding changes concomitant with a volume decrease, with Mn2 bonds to $O3_2$, $O3_3$ (*C2/c*, Fig. 4c) to $O3_2$, $O3_4$ ($P2_1/c$, Fig. 6b) to $O3_1$, $O3_4$ (*C2/c*, Fig. 4b), somewhat like a sequence of steps. This succession of bonding changes is similar to the bonding changes observed in electron density representations of ductile behavior in metal alloys determined by Eberhart (1999, 1996).

The reason for the bond stepping systematics that accompany volume changes almost certainly has to do with (1) anion-anion interaction, which can be studied by an examination of closest-packing systematics, and (2) cation-cation interaction. We can consider the anions in all pyroxene structures as arranged in a distorted closest-packed array (Thompson 1970). One of the ways to decrease the volume is to decrease this distortion. Thompson and Downs (2001) have demonstrated that a major component of volume change in pyroxenes at *T* or at *P* is accomplished through changes in packing distortion. Animations of crystal structures changing with *T* or *P* show that as the volume in a pyroxene changes, there is an apparent shear

of the two neighboring anion monolayers that sandwich the M1 and M2 cations, such that the upper level in Figure 2 moves toward the top of the figure and the lower level moves to the bottom (Downs et al. 1999b). This is manifest by the rotation of the tetrahedra and change in Si-O-Si bridging angles or O3-O3-O3 angles, as well as the change in the β angle of the monoclinic phases. As the bridging O3 atoms shift their positions, the M2-O3 distances change and the relative displacements can result in bonds forming or breaking. An example of this sort of bonding change is found in kosmochlor, $NaCrSi_2O_6$, at pressure, where Na goes from six- (Fig. 4c) to eight-coordinated (Fig. 4d) (Origlieri et al. 2001). The bonding change most likely also occurs in other Na-bearing pyroxenes such as acmite or jadeite at sufficient pressure.

The only cation-cation distance that can change from one ideal pyroxene to another is between M2 and Si (Thompson and Downs 2003). In *C2/c* pyroxenes with M2 bonded to $O3_2$ and $O3_3$ (the most common ambient condition monoclinic topology), an individual M2 polyhedron is observed to share 2 edges with tetrahedra (Fig. 4c) and thus this pyroxene has two high-energy, short M2-Si separations (Sueno et al. 1976). This distance is observed to decrease with decreasing volume, for example, the Na-Si separation in kosmochlor (Origlieri et al. 2001) shortens from 3.00 Å at P = 0 GPa to 2.92 Å at P = 9.75 GPa, leading to further increase in lattice energy. Thus the decrease in packing distortion leads to an increase in cation-cation repulsion. Consequently, the $O3_3$ atoms shift their positions, the M2-$O3_3$ bond breaks, and in some cases, an M2-$O3_4$ bond forms. Thus M2 loses its twofold symmetry, resulting in a structure with one shared edge between the M2 polyhedron and the tetrahedra (Fig. 6), and a reduction in symmetry to $P2_1/c$.

Without significant change in the compression mechanism, further reduction of cell volume coincides with additional shearing of the monolayers and if the coordination number of M2 was only five, then it will go to six, as observed in Table 1 for spodumene from P = 3.34 GPa to P = 8.84 GPa (Arlt and Angel 2000). The energetics related to further volume decrease involves overcoming the one remaining repulsive M2-Si interaction, and so the M2-$O3_2$ bond breaks and an M2-$O3_1$ bond forms, and the crystal goes back to *C2/c* symmetry, but with no shared edges (Fig. 4b). According to Thompson and Downs (2003) this topology exhibits the lowest energy form for an ideal pyroxene and the packing is CCP.

With respect to the bonding topology around M2, the transformations that involve orthorhombic pyroxenes are similar to the transformations of pyroxenes with monoclinic symmetry because *Pbca* is similar to $P2_1/c$ and *Pbcn* is similar to *C2/c*. For instance, ferrosilite with *Pbca* symmetry transforms to a twinned *C2/c* with pressure (Hugh-Jones et al. 1996). The *Pbca* structure has one shared edge between the M2 polyhedron and a tetrahedron (Fig. 7), just like the $P2_1/c$ structure (Fig. 6). This distance also decreases with increasing pressure. The Mg2-Si separation in enstatite (Hugh-Jones and Angel 1994) decreases from 2.81 Å at P = 0 GPa to 2.75 Å at P = 8.1 GPa. Also, the anions move in a way that is similar to their movement in clinopyroxenes at pressure. Thus the M2-$O3_2$ bond that is associated with the shared edge breaks, and a new M2-$O3_1$ bond forms. This topological change puts M2 onto a twofold, which is not consistent with the octahedral stacking sequences of the *Pbca* pyroxenes. Thus the structure must go to *C2/c* with M2 bonds to $O3_1$ and $O3_4$ (Fig. 4b). In a solid-state transformation the octahedral stacking sequence does not need to change, and the *C2/c* phase is twinned. While the transformation is observed in ferrosilite at pressure (Hugh-Jones et al. 1996), it has only been inferred in enstatite (see Hugh-Jones and Angel 1994). Again, in a similar way to the clinopyroxenes, when the volume increases in a *Pbca* pyroxene, it then transforms to *Pbcn* or *C2/c* where M2 is bonded to $O3_2$ and $O3_3$.

Yang et al. (1999) observed that the symmetry of *Pbcn* protopyroxene $Mg_{1.54}Li_{.23}Sc_{.23}Si_2O_6$ changes to $P2_1cn$ with increasing pressure. A meaningful electron density cannot be computed for this phase because of the mixed occupancy of the M1 and M2 sites. However, the bond lengths indicate that the $P2_1cn$ phase has M2-$O3_2$ and M2-$O3_4$ bonds, just like $P2_1/c$, but with no change in the octahedral stacking sequence from the *Pbcn* phase. Thus, this phase transforms along the same sequence of M2-O3 bond steps as is observed in the *C2/c* – $P2_1/c$ transformations.

BONDING IN THE "ANTIPHASE DOMAINS" OF PIGEONITE AND CLINOENSTATITE

Clinopyroxenes of composition $(Fe,Mg,Ca)_2Si_2O_6$ often contain antiphase domains that are related by $(a + b)/2$ translation with Ca atoms at the boundaries (Morimoto and Tokonami 1969). Crystals, especially those of volcanic origin, that display these features have sharp (a)-type reflections ($h + k$ even) while the (b)-type reflections ($h + k$ odd) are diffuse, or in other words, have greater half-widths, in the **a*b*** plane. The results of the present study support the interpretation of Morimoto and Tokonami (1969), and also provide bonding details. Suppose that we examine the bonding around the (Mg,Fe)2 sites along the *c*-direction (Fig. 9). Then the bonding would be to $O3_2$ and $O3_4$, until we came across, say, a Ca atom. Then the Ca atom would be bonded to all four O3 atoms. If, on the one hand, the

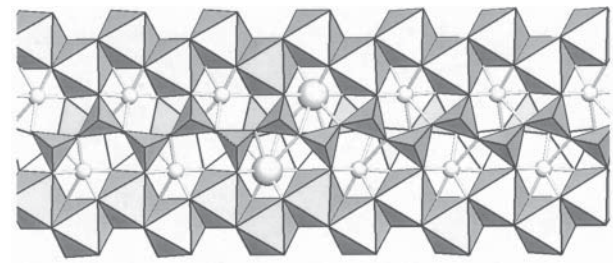

FIGURE 9. An illustration of the bonding near the boundary of an antiphase domain. The (Mg,Fe)2 atoms, depicted as smaller spheres, are bonded to two bridging O3 atoms, as illustrated in Figure 7b. The Ca2 atoms, depicted as larger spheres, are bonded to four bridging O3 atoms, as illustrated in Figure 4d. If a Ca atom were on the boundary of an antiphase domain then the (Mg,Fe)2 atoms on either side of the Ca2 atom would be bonded to different pairs of bridging O3 atoms, with little disruption of the structure. The shift in the bonding of the (Mg,Fe)2 atoms at the antiphase boundary is considered tantamount to an exchange of SiA and SiB chains, not by any actual translation of $(a + b)/2$ but by a slight displacement of atoms in the chains.

Ca atom were on the boundary of the antiphase domain then the following (Mg,Fe)2 atoms would be bonded to $O3_1$ and $O3_3$ with little disruption of the structure, and consequently little energy penalty. If, on the other hand, the following (Mg,Fe)2 atoms were still bonded to $O3_2$ and $O3_4$ then the Ca atom would not be on an antiphase boundary. The shift in the bonding of the(Mg,Fe)2 atoms at the antiphase boundary is considered tantamount to an exchange of SiA and SiB chains, not by any actual translation of $(a + b)/2$ but by a slight displacement of atoms in the chains (Morimoto and Tokonami 1969). It follows that the diffuse ($h + k$ odd) peaks are more likely to be a consequence of Ca-composition rather that cooling history (Smyth 1974b). Images constructed by electron microscopy have demonstrated that these sorts of antiphase boundaries are a relatively common feature of pyroxenes (Buseck and Iijima 1975).

ACKNOWLEDGEMENTS

Mark Welch, and two anonymous reviewrs are thanked for their constructive reviews. The National Science Foundation is gratefully acknowledged for funding this study through EAR-9903104, Compression Mechanisms of Upper Mantle Minerals.

REFERENCES CITED

Allan, D.R. and Nelmes, R.J. (1996) The structural pressure dependence of potassium titanyl phosphate (KTP) to 8 GPa. Journal of Physics, Condensed Matter, 8, 2337–2363.

Angel, R.J., Chopelas, A., and Ross, N.L. (1992) Stability of high-density clinoenstatite at upper-mantle pressures. Nature, 358, 322–324.

Arlt, T. and Angel, R.J. (2000) Displacive phase transitions in C-centred clinopyroxenes: Spodumene, $LiScSi_2O_6$ and $ZnSiO_3$. Physics and Chemistry of Minerals, 27, 719–731.

Arlt, T. and Armbruster, T. (1997) The temperature-dependent $P2_1/c$-$C2/c$ phase transition in the clinopyroxene kanoite MnMg [Si_2O_6]: a single-crystal X-ray and optical study. European Journal of Mineralogy, 9, 953–964.

Arlt, T., Angel, R.J., Miletich, R., Armbruster, T., and Peters, T. (1998) High-pressure $P2_1/c$-$C2/c$ phase transitions in clinopyroxenes: Influences of cation size and electronic structure. American Mineralogist, 83, 1176–1181.

Bader, R.F.W. (1990) Atoms in molecules. Oxford Science Publications, Oxford, U.K.

———(1998) A bond path: A universal indicator of bonded interactions. Journal of Physical Chemistry, 102A, 7314–7323.

Bragg, W.L., Claringbull, G.F., and Taylor, W.H. (1965) Crystal Structure of Minerals. Cornell University Press, Ithaca, New York, 409 pages.

Brown, I.D. (2002) Topology and chemistry. Structural Chemistry, 13, 339–355.

Buseck, P.R. and Iijima, S. (1975) High resolution electron microscopy of enstatite. II: Geological application. American Mineralogist, 60, 771–784.

Cameron, M. and Papike, J.J. (1981) Structural and chemical variations in pyroxenes. American Mineralogist, 66, 1–50.

Cameron, M., Sueno, S., Prewitt, C.T., and Papike, J.J. (1973) High-temperature crystal chemistry of acmite, diopside, hedenbergite, jadeite, spodumene, and ureyite. American Mineralogist, 58, 594–618.

Clark, J.R., Appleman, D.E., and Papike, J.J. (1969) Crystal-chemical characterization of clinopyroxenes based on eight new structure refinements. Mineralogical Society of America Special Paper, 2, 31–50.

Coe, R.S. and Kirby, S.H. (1975) Orthoenstatite to clinoenstatite transformation by shearing and reversion by annealing – mechanism and potential applications. Contributions to Mineralogy and Petrology, 52, 29–55.

Coppens, P. (1997) X-ray Charge Densities and Chemical Bonding. IUCr Texts on Crystallography, Oxford Science Publications, Oxford.

Deer, W.A., Howie, R.A., and Zussman, J. (1997) Rock-Forming Minerals. Single Chain Silicates, 668 p. Wiley, New York.

Downs, R.T., Teter, D.M., and Gibbs, G.V. (1997) A pro-crystal electron density analysis of potassium-oxygen bonding in microcline and KTP as a function of pressure. EOS Transactions, AGU, Fall Meeting Supplement, 78 (46) F754

Downs, R.T., Yang, H., Hazen, R.M., Finger, L.W., and Prewitt, C.T. (1999a) Compressibility mechanisms of alkali feldspars: New data from reedmergnerite. American Mineralogist, 84, 333–340.

Downs, R.T., Gibbs, G.V., and Boisen M.B. Jr. (1999b) Topological analysis of the $P2_1/c$ to $C2/c$ transition in pyroxenes as a function of temperature and pressure. EOS Transactions, AGU, Fall Meeting Supplement, 80 (46) F1140.

Downs, R.T., Gibbs, G.V., Boisen, M.B. Jr., and Rosso, K.M. (2002) A comparison of bond critical point properties from procrystal and *ab initio* model representations of electron density distributions of minerals. Physics and Chemistry of Minerals, 29, 369–385.

Eberhart, M.E. (1999) Why things break. Scientific American, 281, 66.

———(1996) The metallic bond: Elastic properties. Acta Materialia, 44, 2495–2504.

Finger, L.W. and Ohashi, Y. (1976) The thermal expansion of diopside to 800 °C and a refinement of the crystal structure at 700 °C. American Mineralogist, 61, 303–310.

Flesch, L.M., Li, B., and Liebermann, R.C. (1998) Sound velocities of polycrystalline $MgSiO_3$-orthopyroxene to 10 GPa at room temperature. American Mineralogist, 83, 444–450.

Ghose, S., Schomaker, V., and McMullan, R.K. (1986) Enstatite, $Mg_2Si_2O_6$: A neutron diffraction refinement of the crystal structure and a rigid-body analysis of the thermal vibration. Zeitschrift für Kristallographie, 176, 159–175.

Gibbs, G.V., Boisen, M.B., Jr., Beverly, L.L., and Rosso, K.M. (2001) A computational quantum chemical study of the bonded interactions in earth materials and structurally and chemically related molecules. In R.T. Cygan and J.D. Kubicki, Eds., Molecular modeling theory: Applications in the Geosciences, vol. 42, p. 345–382. Reviews in Mineralogy and Geochemistry, Mineralogical Society of America, Washington, D.C.

Hawthorne, F.C. and Grundy, H.D. (1973) Refinement of the crystal structure of $NaScSi_2O_6$. Acta Crystallographica, B29, 2615–2616.

——— (1974) Refinement of the crystal structure of $NaInSi_2O_6$. Acta Crystallographica, B30, 1882–1884.

———(1977) Refinement of the crystal structure of $LiScSi_2O_6$ and structural variations in alkali pyroxenes. Canadian Mineralogist, 15, 50–58.

Hugh-Jones, D. and Angel, R.J. (1994) A compressional study of $MgSiO_3$ orthoenstatite up to 8.5 GPa. American Mineralogist, 79, 405–410.

Hugh-Jones, D., Woodland, A., and Angel, R. (1994) The structure of high-pressure $C2/c$ ferrosilite and crystal chemistry of high-pressure $C2/c$ pyroxenes. American Mineralogist, 79, 1032–1041.

Hugh-Jones, D., Sharp, T., Angel, R., and Woodland, A. (1996) The transition of orthoferrosilite to high-pressure $C2/c$ clinoferrosilite at ambient temperature. European Journal of Mineralogy, 8, 1337–1345.

Ito, T. (1950) X-ray studies on polymorphism. Maruzen, Tokyo, 231 p.

Jayaraman, A., Shieh, S.R., Sharma, S.K., Ming, L.C., and Wang, S.Y. (2001) Pressure-induced phase transitions in $CuGeO_3$ from Raman spectroscopic studies. Journal of Raman Spectroscopy, 32, 167–175.

Kanzaki, M. (1991) Ortho/clinoenstatite transition. Physics and Chemistry of Minerals, 17, 726–730.

Kuntzinger, S., Dahaoui, S., Ghermani, N.E., Lecomte, C., and Howard, J.A.K. (1999) The use of CCD area detectors in charge-density research. Application to a mineral compound: the a-spodumene $LiAl(SiO_3)_2$. Acta Crystallographica, B55, 867–881.

Levien, L. and Prewitt, C.T. (1981) High-pressure structural study of diopside. American Mineralogist, 66, 315–323.

Morimoto, N., and Tokonami, M. (1969) Domain structure of pigeonite and clinoenstatite. American Mineralogist, 54, 725–740.

Morimoto, N., Appleman, D.E., and Evans Jr., H.T. (1960) The crystal structures of clinoenstatite and pigeonites. Zeitschrift für Kristallographie, 114, 120–147.

Morimoto, N., Nakajima, Y., Syono, Y., Akimoto, S., and Matsui, Y. (1975) Crystal structures of pyroxene-type $ZnSiO_3$ and $ZnMgSi_2O_6$. Acta Crystallographica, B31, 1041–1049.

Murakami, T., Takéuchi, Y., and Yamanaka, T. (1982) The transition of orthoenstatite to protoenstatite and the structure at 1080 °C. Zeitschrift für Kristallographie, 160, 299–312.

——— (1984) X-ray studies on protoenstatite II. Effect of temperature on the structure up to near the incongruent melting point. Zeitschrift für Kristallographie, 166, 263–275.

Ohashi, H. (1984) Polysynthetically-twinned structures of enstatite and wollastonite. Physics and Chemistry of Minerals, 10, 217–229.

Ohashi, H., Osawa, T., and Sato, A. (1994) $NaScSi_2O_6$. Acta Crystallographica, C50, 838–840.

Ohlert, J.M. and Chopelas, A. (1999) $C2/c$ to $C2/c$ phase transition in diopside at high pressure. Transactions of the American Geophysical Union, 80, F928.

Origlieri, M.J., Downs, R.T., and Harlow, G.E. (2001) Compression mechanism of the pyroxene kosmochlor. EOS Transactions, AGU, Fall Meeting Supplement, 82 (47) F1393.

Pannhorst, W. (1981) Comparison between topological classifications of pyroxenes. Neues Jahrbuch für Mineralogie Abhandlungen, 143, 1–14.

Papike, J.J., Prewitt, C.T., Sueno, S., and Cameron, M. (1973) Pyroxenes: Comparisons of real and ideal structural topologies. Zeitschrift für Kristallographie, 138, 254–273.

Prencipe, M., Tribaudino, M., Pavese, A., Hoser, A., and Reehuis, M. (2000) A single-crystal neutron-diffraction investigation of diopside at 10 K. Canadian Mineralogist, 38, 183–189.

Redhammer, G.J., Roth, G., Paulus, W., André, G., Lottermoser, W., Amthauer, G., Treutmann, W., and Koppelhuber-Bitschnau, B. (2001) The crystal and magnetic structure of Li-aegirine $LiFe^{3+}Si_2O_6$: a temperature-dependent study. Physics

and Chemistry of Minerals, 28, 337–346
Sasaki, S., Takéuchi, Y., Fujino, K., and Akimoto, S. (1982) Electron-density distributions of three orthopyroxenes, $Mg_2Si_2O_6$, $Co_2Si_2O_6$, and $Fe_2Si_2O_6$. Zeitschrift für Kristallographie, 158, 279–297.
Sato, A., Osawa, T., and Ohashi, H. (1994) $LiGaSi_2O_6$. Acta Crystallographica, C50, 487–488.
——— (1995) Low-temperature form of $LiGaSi_2O_6$. Acta Crystallographica, C51, 1959–1960.
Shimobayashi, N. and Kitamura, M. (1991) Phase transition in Ca-poor clinopyroxenes. Physics and Chemistry of Minerals, 18, 153–160.
Smith, J.V. (1959) The structure of proto-enstatite, $MgSiO_3$. Acta Crystallographica, 12, 515–519.
Smyth, J.R. (1974a) Experimental study on the polymorphism of enstatite. American Mineralogist, 59, 345–352.
——— (1974b) The high temperature crystal chemistry of clinohypersthene. American Mineralogist, 59, 1069–1082.
Sueno, S., Cameron, M., and Prewitt, C.W. (1976) Orthoferrosilite: High-temperature crystal chemistry. American Mineralogist, 61, 38–53.
Sueno, S., Kimata, M., and Prewitt, C.W. (1984) The crystal structure of high clinoferrosilite. American Mineralogist, 69, 264–269.
Thompson, J.B. Jr. (1970) Geometrical possibilities for amphibole structures: Model biopyriboles. American Mineralogist, 55, 292–293.
Thompson, R.M. and Downs, R.T. (2001) Quantifying distortion from ideal closest-packing in a crystal structure with analysis and application. Acta Crystallographica, B57, 119–127.
——— (2003) Model Pyroxenes I: Ideal Pyroxene Topologies. American Mineralogist, 88, xxx–xxx. RACHEL FILL IN.
Tokonami, M., Horiuchi, H., Nakano, A., Akimoto, S., and Morimoto, N. (1979) The crystal structure of the pyroxene-type $MnSiO_3$. Mineralogical Journal, 9, 424–426.
Tribaudino, M. (2000) A transmission electron microscope investigation of the $C2/c \rightarrow P2_1/c$ phase transition in clinopyroxenes along the diopside-enstatite ($CaMgSi_2O_6$-$Mg_2Si_2O_6$) join. American Mineralogist, 85, 707–715.
Warren, B.E. and Bragg, W.L. (1928) XII. The structure of diopside, $CaMgSi_2O_6$. Zeitschrift für Kristallographie, 69, 168–193.
Warren, B.E. and Modell, D.I. (1930) The structure of enstatite $MgSiO_3$. Zeitschrift für Kristallographie, 75, 1–14.
Yamanaka, T., Hirano, M., and Takéuchi, Y. (1985) A high temperature transition in $MgGeO_3$ from clinopyroxene (*C*2/*c*) type to orthopyroxene (*Pbca*) type. American Mineralogist, 70, 365–374.
Yang, H. and Ghose, S. (1995) High temperature single crystal X-ray diffraction studies of the ortho-proto phase transition in enstatite, $Mg_2Si_2O_6$ at 1360 K. Physics and Chemistry of Minerals, 22, 300–310.
Yang, H. and Prewitt, C.T. (2000) Chain and layer silicates at high temperatures and pressures. Reviews in Mineralogy and Geochemistry, 41, High-Temperature and High-Pressure Crystal Chemistry, Robert M. Hazen and Robert T. Downs, Editors. Mineralogical Society of America, Washington DC.
Yang, H., Finger, L.W., Conrad, P.G., Prewitt, C.T., and Hazen, R.M. (1999) A new pyroxene structure at high pressures: Single crystal X-ray and Raman study of the *Pbcn*-$P2_1cn$ phase transition in protopyroxene. American Mineralogist, 84, 245–256.
Zhang, L., Ahsbahs, H., Hafner, S.S., and Kutoglu, A. (1997) Single-crystal compression and crystal structure of clinopyroxene up to 10 GPa. American Mineralogist, 82, 245–258.

MANUSCRIPT RECEIVED MARCH 5, 2002
MANUSCRIPT ACCEPTED DECEMBER 23, 2002
MANUSCRIPT HANDLED BY MARK WELCH